DEVELOPMENT AND APPLICATION OF A VERTICAL HIGH SPEED MOTOR-COMPRESSOR SIMULATOR FOR ROTOR DROP ONTO AUXILIARY BEARINGS

by

David Ransom
Principal Engineer
Southwest Research Institute
San Antonio, Texas

Andrea Masala
Senior Engineer
GE Oil&Gas
Florence, Italy

Jeffrey Moore
Program Manager
Southwest Research Institute
San Antonio, Texas

Giuseppe Vannini
Senior Design Engineer

Massimo Camatti
Manager, Turbomachinery Mechanical Design, R&D Division
GE Oil&Gas
Florence, Italy

and

Michel Lacour
Spindles Engineering Manager
S2M
St. Marcel, France

David L. Ransom is a Principal Engineer at Southwest Research Institute, in San Antonio, Texas. His professional experience over the last 10 years includes engineering and management responsibilities at Boeing, Turbocare, and Rocketdyne. Mr. Ransom's research interests include rotordynamics, structural dynamics, seals and bearings, finite element analysis, and root cause failure analysis. He has authored 12 technical papers in the field of rotordynamics, thermodynamics, and root cause failure analysis.

Mr. Ransom received his B.S. degree (Engineering Technology, 1995) and M.S. degree (Mechanical Engineering, 1997) from Texas A&M University. He is also a licensed Professional Engineer in the State of Texas.

Andrea Masala is a Senior Engineer, with the GE Oil&Gas Advanced Technology Rotordynamic team, in Florence, Italy. In his current position, his area of activity is on AMB's integration in GE Oil&Gas machines. He has had assignments on the rotating machinery and centrifugal compressor NPI teams as turbomachinery rotordynamic specialist. He is a member of ISO TC108/SC2/ workgroup for ISO14839-4 issue.

Mr. Masala earned his MSc. degree (Mechanical Engineering, 1999) from the University of Cagliari and joined GE in 2002.

Jeffrey Moore is a Program Manager at Southwest Research Institute, in San Antonio, Texas. His professional experience over the last 18 years includes engineering and management responsibilities related to centrifugal compressors and gas turbines at Solar Turbines Inc. in San Diego, California, Dresser-Rand in Olean, New York, and Southwest Research Institute in San Antonio, Texas. Dr. Moore's interests include advanced compression methods, rotordynamics, seals and bearings, computational fluid dynamics, finite element analysis, controls, and aerodynamics. He has authored more than 20 technical papers related to turbomachinery and has given numerous tutorials and lectures. He is currently the vice-chair of the Oil and Gas Committee for IGTI Turbo Expo.

Dr. Moore holds B.S., M.S., and Ph.D. degrees (Mechanical Engineering) from Texas A&M University.

Giuseppe Vannini is a Senior Design Engineer in the Conceptual and Advanced Mechanical Design Department of GE Oil&Gas, in Florence, Italy. He joined the company in early 2001 and has been involved in advanced rotordynamics studies on high performance compressors developing both analytical and experimental research activities. Recently, he extended his activity to the design of prototypes for subsea applications (i.e., multiphase pumps and integrated high speed motor-compressors).

Dr. Vannini holds a Ph.D. degree (Mechanical Engineering) from Pisa University. He is a member of API 684 Task Force in charge of the Rotordynamics Tutorial.

Massimo Camatti is the Manager of Turbomachinery Mechanical Design of the R&D Division of GE Oil&Gas, in Florence, Italy. He joined Nuovo Pignone in 1988. After beginning his career as a centrifugal compressor Design Engineer, Mr. Camatti was then a compressor design leader in several advanced technology projects. Prior to his current position, he covered the roles of Design Manager of centrifugal and axial compressors for liquefied natural gas application and R&D Manager for centrifugal and axial compressor product lines.

Mr. Camatti holds an M.S. degree (Mechanical Engineering) from Florence University.

Michel Lacour is the Spindles Engineering Manager for S2M, in St. Marcel, France, and has been working with S2M in since graduation from college. During his time at S2M, Mr. Lacour has had the opportunity of following the details of the improvement of active magnetic bearing technology and of approaching different applications (turbo molecular pumps, X-ray tubes, electric motors, compressors, water turbines, steam turbines, milling and grinding spindles). For the past 10 years, he has participated in the elaboration of the ISO standard for Active Magnetic Bearings (ISO 14839).

Mr. Lacour holds a degree (Electronic Engineering, 1976) from Ecole Supérieure d'Electricité, Paris.

ABSTRACT

During the conceptual development of a subsea motor-compressor prototype running on active magnetic bearings, the emergency landing on the catcher bearings was identified as a potential technology gap. This is because the rotor in object is vertical and supercritical. A subscale simulator was then developed with the twofold aim to collect useful experimental data for data matching with a numerical simulation (also developed for this special application) and to perform endurance testing of the catcher bearings to understand their mechanical limits.

The selected scale factor was one-third in order to utilize standard size active magnetic bearings and meet the project schedule. The subscale rotor design was aimed to respect the dynamic similitude with the real machine having the same separation between the rotor critical speeds and the operating speed range. Maximum test rig rotor speed is 30,000 rpm. Moreover the test rig casing design simulated also the real casing dynamic behavior.

The test campaign was then divided in two steps. During the first step a test matrix was defined to address all the potential important parameters in the landing dynamics: unbalance magnitude, unbalance distribution (to excite different modes), rotation speed at drop start, duration of the delevitation, type of axes to be delevitated and active magnetic bearings (AMBs) cooling medium. Overall 19 tests were performed. The main outcomes from the test were:

- The rotor always showed a forward cylindrical subsynchronous whirl.
- The whirl behavior was not affected by unbalance level and distribution, landing duration, or drop speed.
- The whirl frequency is not related to any rotor/casing natural frequencies.

The numerical simulation was developed in a numerical computing environment software specifically for the test rig system and was tuned on the basis of the experimental results. A key factor in model tuning was the introduction of a cross coupled term to allow the rotor to follow a forward whirling motion since the beginning of the drop. The physical nature of this cross-coupled force is still to be exactly identified. The final simulation results well matched with the experimental data both in whirling direction and frequency.

Afterward the simulation was extended to the full-scale machine to predict landing behavior during the future full load testing and operation. Simulation shows the machine is stable for nominal conditions and the stability margin is greater than two. Moreover catcher bearing loads are within allowable limits. Finally a sensitivity study was performed showing that decreasing catcher bearings clearances and reducing seal entry swirl will lead to improved stability margin and dynamic loads.

A second step of testing was the endurance test of the catcher bearings to determine the maximum number of landing. For this purpose the same drop speed (30 krpm) and landing duration (10 sec) was used for all the test runs. Several catcher bearings damage indicators were experienced; finally it was evident that the most reliable indications came from the accelerometers mounted on the bearing housing. The endurance test led to the conclusion that the current design of catcher bearings for this rotor configuration allows at least seven safe drops from full speed in conditions, which can be considered similar or even more severe than the real machine scenario.

INTRODUCTION

A hermetically sealed, high speed, high performance motor-compressor for subsea application is in prototype development. As gas field pressures drop and production rates begin to drop, subsea compression becomes a viable option for boosting gas pressure at the wellhead on the ocean floor. Therefore, this unit is designed to operate on the ocean floor, providing natural gas compression for transport to the onshore processing facility. Some of the key design characteristics of the prototype include vertical rotor orientation, a direct coupled motor-compressor shaft, and three radial bearings, two on the motor shaft and one at the bottom of the compressor assembly. This arrangement has certain advantages with respect to subsea footprint, contaminant protection, and minimal maintenance of mechanical elements. Figure 1 shows the cross-section view of the subsea prototype unit.

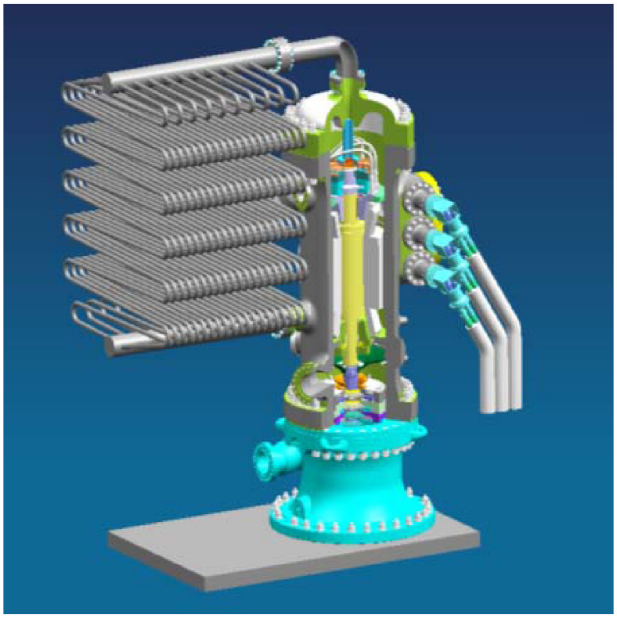

Figure 1. Full Scale Motor-Compressor Unit.

The bearings consist of active magnetic bearings (AMBs) for the primary bearings and preloaded angular contact bearing pairs for the auxiliary (catcher) bearings. Catcher bearings are a critical component because they must endure multiple impact-frictional contact forces with large acceleration, high rotational speed, high radial loads, and must operate in harsh temperature conditions. In addition, during the drop phase, the rotor may experience a lateral self-excited vibration regime (backward/forward whirl), which can produce high dynamic loads on the bearings. In the case of a vertical axis machine, backward/forward whirl regime is even more likely to occur, because gravity load will not contribute to stabilizing the radial motion of the rotor and prevent rotor whirl.

Catcher bearing design and overall machine behavior during the drop phase are recognized as critical issues to get robust machine operation even in the case of AMB failure, and to be able to restart the machine after multiple landings without retrieving the entire unit from the sea bed. Most of landing technical knowledge has been developed for horizontal turbomachinery while only few comparisons between predictions and measurements were performed for vertical units.

A detailed numerical model of vertical rotor drop on two catcher bearings is presented by Sun, et al. (2004), to simulate the dynamics of a flywheel energy storage system on catcher bearings. The radial and axial rotordynamics are combined in a 16 degrees of freedom (DOF) model, including cross-coupled stiffness and gyroscopic effects and study on axial preload, friction coefficients, and unbalance loads is carried out to highlight effects in terms of impact forces, heat generation, and whirl rate prediction.

Experimental results of a 2 MW (2682 hp) vertical flywheel rotor drop on catcher bearings are presented by Caprio, et al. (2004). The 44 drops performed highlight the insurgence of forward motion for all unbalance level and drop speed conditions tested. Internal rotor damping due to friction laminations stacks is proposed as a possible origin of the forward acting force in addition to unbalance excitation. Forward whirl rate of the rotor close to the housing mode suggested a strong effect of the combined rotor/stator system mode in determining the whirl "locking" frequency.

Similar tendency to forward rotor whirling is reported by McMullen, et al. (2006), after an extensive 200 drop testing campaign on a 109 kg (240 lb) vertical flywheel rotor to identify drop dynamics and possible damage mechanism of catcher bearings and rotor.

As reported by Swanson, et al. (1995), the rotor unbalance level is experienced to be a key parameter in promoting the rotor forward whirl. Testing performed by the authors on different auxiliary bearing configurations and support systems shows the positive effects of compliance mounted auxiliary bearings to prevent whirl occurrence.

The behavior of a corrugated ribbon damping system for compliance mounted catcher bearings and effects in terms of rotor drop dynamics are reported by Schmied and Pradetto (1992). The numerical simulations and experimental activity highlight the benefits of radial and circumferential damping introduced by the corrugated ribbon in limiting the whirl frequency and motion. Electromagnetic cross coupling forces due to motor stator and rotor interaction are suggested as possible origin of the unexpected forward rotor whirl experienced during the testing activity.

From the literature above, concern on rotor whirl rate and direction, vibration amplitudes, and catcher bearings damage mechanism is deemed worthy for further study in order to close this technology gap for the vertical rotor drop prediction and identify suitable design solutions to leverage catcher bearing life (even further than API 617, Seventh Edition [2002] expectations). A complete numerical and experimental approach is put in place to get a predictive tool able to analyze prototype performances and drive suitable design solutions. For the purpose of validation, a subscale test rig and simulation are developed to study the whirl response characteristics of this unique motor-compressor arrangement. Following this validation activity, the full scale prototype unit is studied using the previously developed simulation tool. Finally, endurance tests are performed on the subscale test rig to provide some initial indication of anticipated auxiliary bearing life and to evaluate potential auxiliary bearing health indicators that will be necessary for subsea operation.

SUBSCALE TEST RIG

For the purpose of the combined experimental/analytical development program, a test rig is designed, built, and operated to provide much needed experimental results for this unique rotor configuration. The test rig consists of a three bearing rotor, suspended within a vertical casing (Figure 2). The primary bearings provide control of seven axes (six radial and one axial) at three bearing locations. The secondary (Aux) bearings are preloaded pairs of angular contact bearings and are supported in the radial direction by a damper ribbon. The test rig was built at one-third scale of the motor-compressor to minimize cost, but exhibits behavior according to rotordynamic similitude. In order to have rotordynamic similitude, the test rig rotates at up to three times the full scale rotor, or about 30,000 rpm.

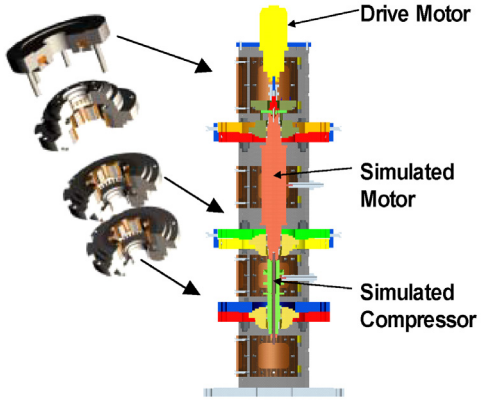

Figure 2. Vertical Landing Test Rig.

The test rig rotor is generally a one-third scale of the full scale unit, using dummy masses to simulate the magnet motor core and the compressor impellers. The test rotor is driven by an induction electric motor using a variable frequency drive (VFD), coupled via

a flexible coupling to the top end of the motor-compressor assembly. This drive motor is used to accelerate the rotor to full speed and also used to slow down the rotor in a controlled fashion, matching as close as possible the anticipated rate of deceleration of the full scale unit. Figure 3 shows a photograph of the completed test rig.

Figure 3. Test Rig Photograph.

In addition to AMB sensors, two additional probe pairs are placed at rotor midspan planes to detect the rotor orbits in these planes. Four velocity transducers located on the casing at the upper and middle bearing plane locations are used to detect the housing dynamics. Transient data are captured using a 24 bit data acquisition system that acquires all 16 channels simultaneously DC coupled in a continuous waveform at 12,000 samples/sec.

The test matrix was designed to vary the following parameters: unbalance magnitude, unbalance distribution (to excite different modes), rotation speed, duration of the delevitation, and which magnetic bearing axes were delevitated. Two unbalance levels were tested, equating to about 4 and 12 times the API unbalance amount (API 617, 2002). Sample experimental results are presented in Figure 4 (adapted from Ransom, et al., 2008). This is a waterfall plot of one of the axes at the top bearing location. All bearing axes exhibit similar behavior.

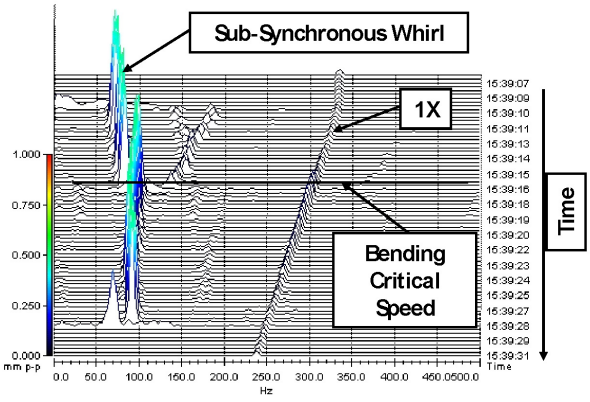

Figure 4. Sample Waterfall Plot—Rotor Passes Through Bending Critical Speed.

Figure 4 shows the results from a drop starting at 20,000 rpm (with 12×API unbalance), and descending through the rotor bending mode at 300 Hz. Relevitation occurs 16 seconds later, at a shaft speed of about 15,000 rpm. The synchronous response (1×) is obvious, ramping from 333 Hz down to 250 Hz. Above the rotor bending frequency, the whirl increases in frequency, ranging from 75 to 85 Hz. At the bending critical, the whirl frequency jumps to 100 Hz, and decays slightly to 90 Hz prior to relevitation. The initial whirl amplitude is 600 µm peak-to-peak (0.024 in peak-to-peak), increasing to 668 µm peak-to-peak (0.027 in peak-to-peak) at the critical speed. Just prior to relevitation, the amplitude is reduced down to 646 µm peak-to-peak (0.025 in peak-to-peak). It is important to note that even with this high level of unbalance, passage through the rotor bending critical is accomplished without difficulty on the auxiliary bearings. Although there is casing mode at 34 Hz, there is no sign of response at this frequency, demonstrating that the whirl frequency is not impacted by the presence of a casing mode within the operating speed range.

SUBSCALE SIMULATION

The present section describes the analytical work performed to simulate the vertical rotor landing activity. This initial simulation is developed to represent the subscale test rig, thus providing the opportunity for validation by direct comparison to experiment. First, the simulation is developed with reduced order finite element models in an effort to reduce simulation time. The models are then coupled using interface force equations, thus providing the flexibility necessary for such nonlinear elements as are included in this simulation. A general discussion of the analysis technique employed is provided by Ransom (2008).

Component Models

The casing model is developed in a fluid flow analysis and design optimization software, and the reduced version is included in the simulation. The rotor model is also developed in the same software and is reduced using the method published by Glasgow and Nelson (1980). The net model size reductions for both models are provided in Table 1. In total, the subscale simulation model is reduced from a size of over 500,000 DOF to just 53 DOF.

Table 1. Model Reduction Results.

Model	Full DOF	Reduced DOF	
	Physical	Physical	Modal
Casing	547,371	13	8
Rotor	378	22	10
Total	***547,749***	***53***	

Figures 5 and 6 show the subscale finite element model for the casing and rotor, respectively. The casing model is shown in both full and reduced form.

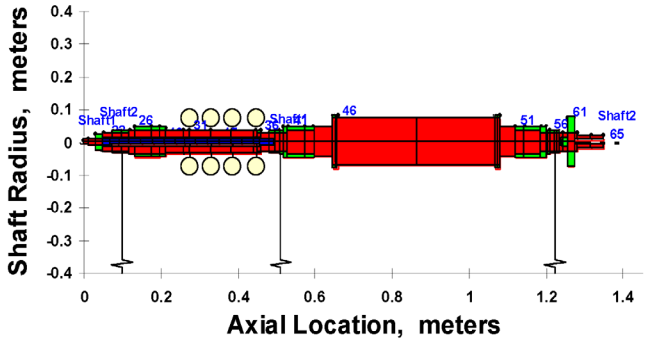

Figure 5. Subscale Rotor Model.

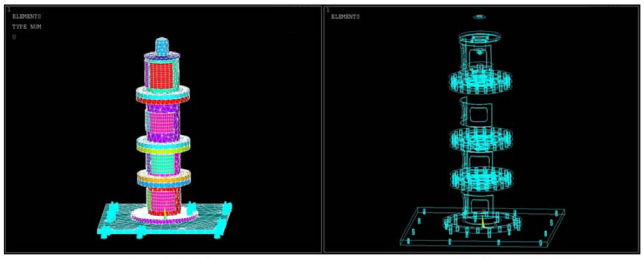

Figure 6. Subscale Casing Model.

As mentioned before, there are three auxiliary bearings in the test rig and each is included in the simulation. The top bearing reacts both thrust and radial loads, while the middle and bottom bearings react only radial loads. The bearing DOF are listed in Table2. These are included in the simulation as independent DOF and are determined from the mass properties of the actual bearing geometry.

Table 2. Catcher Bearing DOF.

Bearing	Component	Sub-Scale DOF
Top Bearing	Inner Race	X,Y,Z, θx
	Outer Race	Y,Z
Middle Bearing	Inner Race	Y,Z, θx
	Outer Race	Y,Z
Bottom Bearing	Inner Race	Y,Z, θx
	Outer Race	Y,Z

The top bearing includes the axial DOF (X), both lateral DOF (Y, Z), and the inner race spin DOF (x) to track the rotational speed of the inner race. The outer race has only the two lateral DOF. The middle and bottom bearings are similar to the top, with the exception of the axial DOF, since there is no thrust reaction at these two bearings. Therefore, the total added DOF to represent the bearings is 16, raising the simulation DOF to 69.

All of the components of the analysis (rotor, casing, and bearings) are assembled into system level matrices and cast into first order form. However, the component matrices remain uncoupled with the connections between independent DOF accomplished via interface forces as outlined by Ransom (2008). The assembled system is solved using readily available first order ordinary differential equation solvers.

The subscale rotor modes are shown in Figure 7. The first rotor bending mode is at 217 Hz, well below the maximum operating speed of 500 Hz. The next relevant mode is the second bending mode at 793 Hz, outside of the operating speed range. The case modes are presented in Figure 8, showing two significant lateral modes within the operating speed range. The lowest mode is the cantilever case mode (35 Hz), in which the entire case moves about the base attachment. The first bending mode of the case is at 210 Hz.

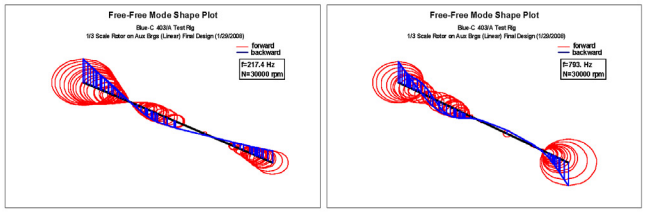

Figure 7. Subscale Rotor Free-Free Modes.

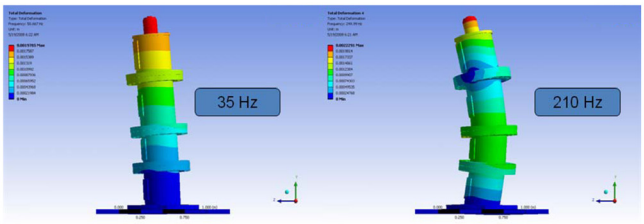

Figure 8. Subscale Case Modes.

Table 3 provides a comparison of the major system natural frequencies for both the subscale and full-scale models. In both cases, the rotor first bending frequency is at about 42 percent of maximum continuous operating speed (MCOS). For the subscale rotor, MCOS is 30,000 rpm while for the full-scale rotor, MCOS is 10,160 rpm. The cantilever case mode for both cases is very low in the speed range, between 4 and 7 percent of MCOS. The most significant difference is the case first bending mode. The full-scale machine has a much lower frequency (compared to MCOS), which is most likely driven by the soft support at the base of the motor-compressor case.

Table 3. Natural Frequency Comparison.

Mode	Sub-Scale		Full-Scale	
	Frequency (Hz)	%MCOS	Frequency (Hz)	%MCOS
Rotor 1st Bending	217	43%	75	44%
Case Cantilever	35	7%	6	4%
Case 1st Bending	210	42%	36	21%

Interface Force Equations

Central to the success of the simulation is the calculation of the interface forces between the various simulation components. Figure 9 is a graphical representation of the auxiliary bearing assembly. The pair of preloaded angular contact bearings comes in direct contact with the rotating shaft. This bearing pair is mounted within a preloaded ribbon damper, which is exaggerated in size for illustration purposes. Finally, the ribbon damper is mounted in a bearing housing that is bolted to the machine case.

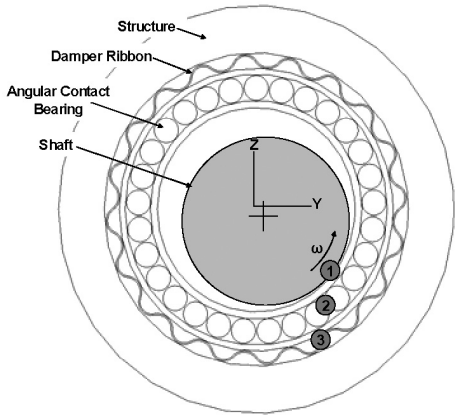

Figure 9. Auxiliary Bearing Assembly. (S2M Patent)

There are three interface force locations considered in this simulation. First, at position one, there is direct contact between the rotor and the inner race. This contact results in both radial and tangential forces on both components. The radial interface force is calculated in Equation (1) using Hertzian theory as presented by Harris (1984):

$$F_{R\_Hz} = \sqrt{\frac{K_D y^3}{\lambda_{hz}^3 C_E^2}} \quad (1)$$

Where K_D and λ_{hz} are functions of geometry, C_E is a function of material properties, y is the relative motion between the two bodies, and F_{R_Hz} is the interface force between the two bodies. The tangential component is dependent on the relative rotation of the inner race and the shaft. If there is a difference in shaft spin speed, there is a net tangential force transmission. However, if the two speeds are equal (within a specified tolerance), the rolling contact condition is applied, as shown in Equation (2).

$$F_{T\_Hz} = \begin{cases} \omega_{IR} < \omega_{Rotor}, \mu_d F_{R\_Hz} \\ \omega_{IR} > \omega_{Rotor}, -\mu_d F_{R\_Hz} \\ \omega_{IR} = \omega_{Rotor}, 0 \end{cases} \quad (2)$$

The interface forces at position two are determined from the angular contact bearing load/deflection curve (Figure 10). This curve includes the compliance of the angular contact bearing as well as additional compliance due to the kinematics of the bearing preload technique.

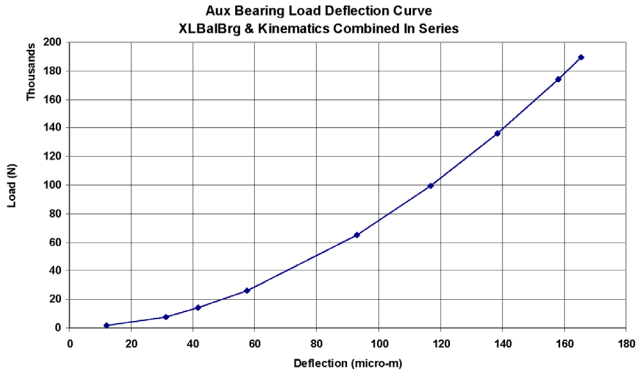

Figure 10. Subscale Catcher Bearing Load Deflection Curve.

The third interface (position three) involves a somewhat bilinear stiffness with radial and tangential components. For the range of damper ribbon radial motion, the radial and tangential forces are calculated from a complex stiffness of the form shown in Equation (3):

$$F_{Dmpr} = yk_0(1 + i\xi) \quad (3)$$

Where k_0 is a function of ribbon geometry, and ξ represents the anticipated coefficient of friction. The real portion of this force is in the radial direction while the imaginary component is in the tangential direction, opposing whirl. Clearly, the tangential component only has meaning when the outer race is whirling. Therefore, a condition is applied such that the tangential term must oppose the tangential velocity vector at any point in time.

Once the damper ribbon is fully compressed, the radial reaction force is the sum of the fully compressed damper spring force (real component) and the Hertzian contact force from the ribbon contact between the outer race and the bearing housing. This radial component is calculated using the same method as presented in Equation (1). The tangential force is still determined by the imaginary component of Equation (3).

Another important interaction that must be captured is the axial/radial coupling that occurs at the thrust bearing location. When the rotor is in contact axially with the top bearing, there is an additional lateral friction force that tends to resist radial motion. The magnitude of the force depends on the interface force between the rotor and the bearing and the coefficient of friction at this same interface. There are three sources of compliance in the axial direction. First, there is Hertzian contact stiffness between the rotor and the thrust bearing inner race. This is modeled similar to Sun, et al. (2004), in Equation (4):

$$K_{X\_hz} = \frac{E\sqrt{\pi\left(r_{ir}^2 - r_{or}^2\right)}}{0.96\left(1-\nu^2\right)} \quad (4)$$

Where E is material modulus, r_{ir} and r_{or} are the inner race inside and outside radii, respectively, and ν is the material Poisson's ratio.

Secondly, the auxiliary bearing is supported axially by the preload spring with a known spring rate. Finally, the structure supporting the auxiliary bearing is also compliant. At each step of the integration, the resulting friction force at this interface is calculated and applied opposite to the direction of motion of the rotor. In this way, the coupling between the axial and lateral directions is achieved.

As described above, the spin speed of each auxiliary bearing inner race is important to the tangential force calculations. Therefore, it is important to include the effects of bearing drag torque and rotor/race interface torque. The drag (bearing friction) torque is modeled based on Harris (1984) in Equation (5):

$$T_d = f_1\left(0.9F_a\, cot(\alpha) - 0.1F_r\right)d_m \quad (5)$$

Where f_1 is a bearing design factor, F_a is the axial load, F_r is the radial load, α is the contact angle, and d_m is the bearing pitch diameter. The friction torque is determined from the radial interface force between the rotor, the inner race, and the coefficient of friction.

SIMULATION COMPARISON TO EXPERIMENTAL RESULTS

This section contains comparative results from both the subscale experimental program and the numerical simulation. The first point of comparison is the initial drop sequence, in which the rotor is free to travel through space until reaching the mechanical elements of the system. A vertical rotor lacks the radial gravity force that tends to suppress whirl. Figure 11 shows the initial drop trajectory for a drop speed of 21,500 rpm. The experimental results show that the rotor initially heads in the counterclockwise (CCW) direction, consistent with the direction of spin. Additionally, it is clear from the orbit plot that the rotor proceeds directly into a forward whirl pattern, even after the very initial contact with the auxiliary bearings. The time duration represented by the orbit is 0.32 seconds, and the rotor establishes a whirl pattern in this period of time. In contrast, the simulation shows very little progression into whirl during the same period of time, and in fact shows the formation of backward whirl as the rotor makes contact with the auxiliary bearings.

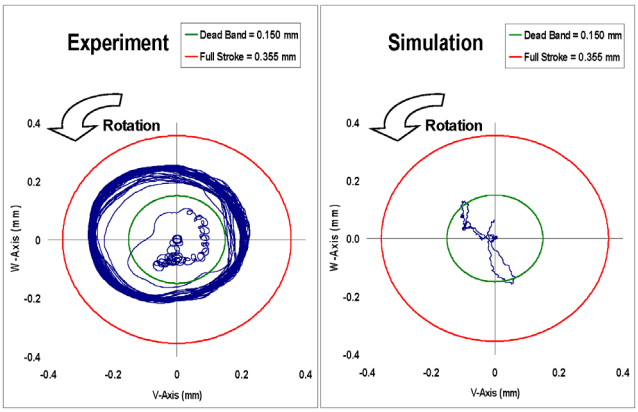

(a) (b)

Figure 11. Comparison of Initial Drop Transient from a) Experiment and b) Simulation.

The second point of comparison between the simulation and the experiment is the established whirl frequency. Figure 12 provides a direct comparison between experiment (top pane) and simulation (bottom pane) for a case in which the rotor is dropped from 21,500 rpm (358 Hz). The experimental results clearly demonstrate subsynchronous whirl starting at about 70 Hz, progressing to 90 Hz by the end of the test period. Further inspection reveals this whirl to be always forward, as shown above in Figure 11. At the end of five seconds, the rotor is relevitated and all of the subsynchronous whirl is eliminated.

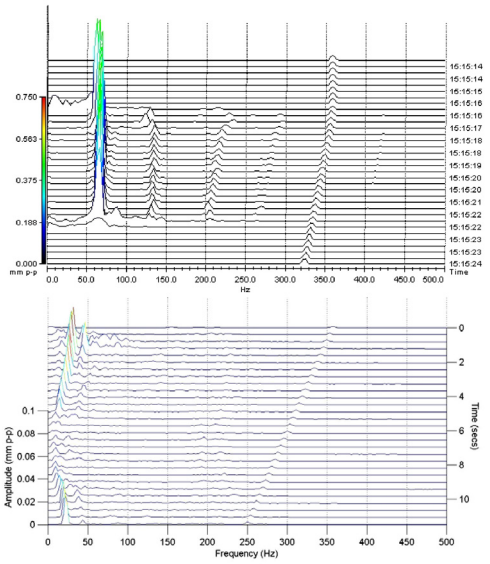

Figure 12. Comparison of Experiment (top) and Simulation (bottom) Waterfall Plots.

The simulation, on the other hand, demonstrates a very different subsynchronous whirl frequency behavior. Initially the rotor whirls at about 25 Hz, but the whirl is found to be backward, due mainly to the friction at the contact between the spinning rotor and the initially static bearing races. As the simulation progresses, the whirl drops to zero frequency, and then transitions into forward whirl with a frequency of about 20 Hz by the end of the simulation.

It is clear from this comparison that there is a force acting upon the rotor in the test rig that is not yet included in the simulation. The experimental results indicate the presence of a forward tangential force similar to that resulting from a positive cross-coupled stiffness. In an effort to determine the value of this unmodeled force, a cross-coupled stiffness parametric study is performed. Figure 13 contains the results of this study, showing the increasing whirl frequency with increasing cross-coupled stiffness. Naturally, all of these cases result in forward whirl due to the strong forward tangential force generated by the applied cross-coupled stiffness. The results of this parametric study suggest that the apparent cross-coupled stiffness in the test rig is on the order of 2.7 MN/m (15.4 klbf/in).

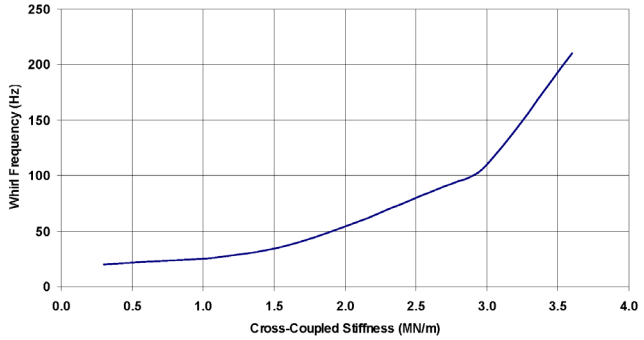

Figure 13. Cross-Coupled Stiffness Parametric Study.

Some initial investigations are made into likely sources of cross-coupled stiffness such as gas forces, gyroscopic forces excited by unbalance, asymmetric tangential contact forces at the thrust bearing, and internal friction at shrink fit locations. All attempts to quantify the gas forces are inconclusive, mainly due to the lack of either significant hydrostatic or hydrodynamic force components and the application of existing tools not designed or validated for such low gas pressures.

Gyroscopic terms are included in the rotor model but should only be important for conical rotor motion. In other words, gyroscopic damping terms are best modeled as cross-coupled damping in the yaw and pitch directions, which clearly require conical motion. However, all of the observed rotor whirl is purely cylindrical, negating the influence of conical whirl components.

Other influences such as internal friction and asymmetric tangential forces at the thrust interface are considered as the most reasonable cause. Just as an order of magnitude check, it is found that using Equations 1-43 from Vance (1988), the predicted cross-coupled stiffness from internal friction is in the range necessary for forward whirl. Equation (6) relates the cross-coupled stiffness to the rotor bending stiffness and is dependent on the value of the internal damping ratio. Typical values for shafts with shrunk on components are around 0.025.

$$\frac{K}{k} = 2\xi_i \frac{\omega}{\omega_n} \tag{6}$$

Where K is the cross-coupled stiffness, k is the rotor bending stiffness, ξ_i is the internal damping ratio, ω is the whirl frequency, and ω_n is rotor undamped natural frequency. Figure 14 shows a plot of the calculated cross-coupled stiffness as a function of rotor whirl frequency. In the range of 90 Hz, the cross-coupled stiffness is around 2.75 MN/m (15.7 klbf/in). Although this is a convenient match with the required value in Figure13, it still remains to develop a nonlinear model that incorporates the physical features of the shrink fits of the actual rotor.

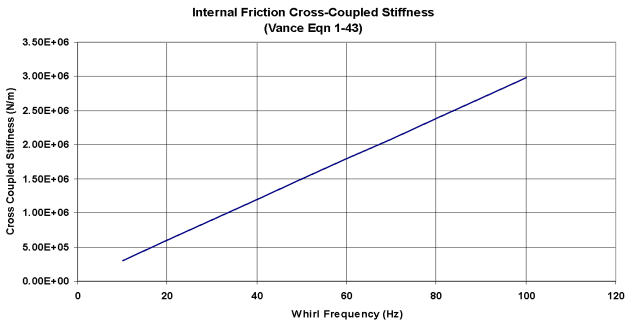

Figure 14. Cross-Coupled Stiffness from Internal Friction.

Another important point to be considered is the magnitude of the unmodeled forward tangential force in comparison to forces typically found in industrial rotating machinery. Through parametric study, it is determined that the forward tangential force is nearly equivalent to a cross-coupled stiffness of 2.7 MN/m (15.4 klbf/in). This stiffness value is on the order of what is typically predicted for eye seals, canned bearing clearances, etc. In other words, in a real gas moving machine, the unmodeled forward tangential force is insignificant compared to the other sources of forward tangential force. Therefore, it is determined that the simulation tool is still useful for the study of the full scale machine, keeping in mind this possible level of uncertainty on the applied cross-coupled stiffness values.

FULL-SCALE SIMULATION

The objective of the full-scale simulation is to support the design of the full-scale machine and, where necessary, guide design decisions to minimize catcher bearing load, thus maximizing

catcher bearing life. Unlike the subscale test rig, the full-scale machine has various hydrodynamic and aerodynamic components that are known to contribute linear stiffness and damping terms to the rotor-bearing system. These include the canned AMBs (which operate with long, smooth annular clearances), all of the impeller eye seals, the impeller shroud aerodynamics, and a honeycomb (HC) damper seal. The approximate locations of each of these components along the rotor are shown in Figure15.

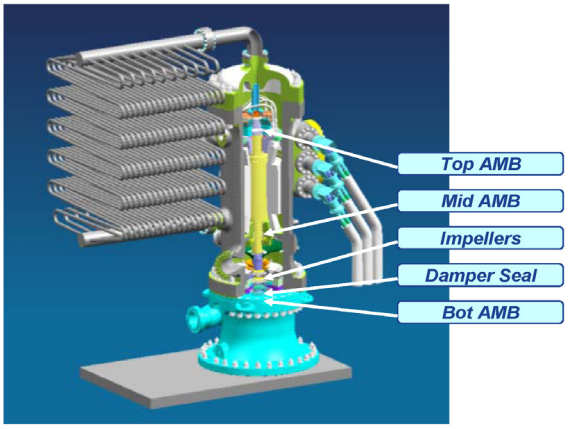

Figure 15. Full-Scale Rotor Node Locations.

Design Case Simulation Results

The full scale simulation is performed first with all parameters at their predicted design values. These includes parameters such as friction coefficients, catcher bearing preload, unbalance mass, damper ribbon performance, catcher bearing clearance, and applied cross-coupled stiffness.

Table 4 lists the baseline values for each of these important parameters. The friction coefficients apply to the rotor-bearing contacts at the three bearing locations. The preloads for the top and middle bearings are identical while the bottom bearing is smaller and requires a lower preload. The unbalance mass is distributed across three rotor planes, matching the shape of the rotor first bending mode. The damper friction coefficient corresponds to damper energy dissipation performance. The net cross-coupled stiffness is the result of combining all impeller eye seal, damper seal, impeller shroud, and canned AMB force coefficients in a modally weighted sum. All of the seal and impeller coefficients are speed dependent, as the compressor stage performance varies with speed during this transient shutdown event. Notice that the sum of all the cross-coupled stiffness values is significantly larger than the cross-coupled stiffness required to make the subscale test rotor demonstrate forward whirl in simulation.

Table 4. Design Case System Parameters.

Parameter	Value
Coefficient of Friction (Static/ Dynamic)	0.30/ 0.15
Catcher Bearing Preload (Top & Middle/ Bottom)	7,620 N/ 2,365 N (1,713 lbf/ 532 lbf)
Unbalance Mass	8xAPI
Damper Friction Coefficient	0.15
Net Cross-Coupled Stiffness	65 MN/m (371 klbf/in)

The net cross-coupled stiffness value includes the predicted contribution from the aerodynamic excitation term, which was evaluated according to a proposed method by the lead author's company (Moore, et al., 2007) and not according to API 617 (2002):

$$K_{xy} = \frac{C_{mr}\ \rho_{dis}\ U^2\ L_{shr}}{Q/Q_{design}} \quad (7)$$

where:

K_{xy} = Cross-coupled stiffness of impeller (N/m or lb/in)
C_{mr} = Impeller cross-coupling coefficient
= 4.0 (SI units) /8.63e-4 (US customary units)
ρ_{dis} = Discharge density (kg/m^3 or lbm/ft^3)
U = Impeller tip speed (m/s or ft/s)
L_{shr} = Axial length of shroud from impeller eye seal to impeller tip (m or in)
Q/Q_{design} = Flow relative to design flow

Note that C_{mr} is dimensionless in SI (Metric) units. This coefficient is constant for a given impeller geometry, but can vary somewhat depending on the detail geometry of the impeller and shroud passage. Equation (7) states that the cross-coupling is proportional to the dynamic pressure (ρ_{dis} U^2) and the shroud length (L_{shr}). The cross-coupling is inversely proportional to relative flow due to the change in the exit flow angle of the impeller. Calculated values using the proposed method by the lead author's company are provided in Table 5.

Table 5. Impeller Cross-Coupled Stiffness.

Parameter	Units SI (US Customary)	Stage 1		Stage 2		Stage 3		Stage 4	
Cmr	n/a (ft-lbf-sec2/lbm-in2)	4.00	(8.63E-04)	4.00	(8.63E-04)	4.00	(8.63E-04)	4.00	(8.63E-04)
ρ-dis	kg/m3 (lbm/ft3)	63.43	(3.96)	73.61	(4.60)	84.55	(5.28)	95.57	(5.97)
U	m/sec (ft/sec)	240	(788)	240	(788)	240	(788)	240	(788)
Lshr	m (in)	0.080	(3.152)	0.084	(3.310)	0.082	(3.231)	0.076	(2.994)
Q/Qdes	n/a	0.789	(0.789)	0.751	(0.751)	0.736	(0.736)	0.720	(0.720)
Kxy stage	N/m (lbf/in)	1.48E+06	(8.47E+03)	1.90E+06	(1.08E+04)	2.17E+06	(1.24E+04)	2.32E+06	(1.33E+04)
Total	N/m (lbf/in)							**7.87E+06**	**(4.50E+04)**

Figure 16 documents the results of the design case simulation. As shown in the overall time history results, the relative motion of the rotor remains within the compliant portion of the ribbon dampers (red circle indicates limit of compliant range) indicating minimal loading on the catcher bearings. In addition, all three bearings quickly accelerate to full rotor speed, evidence of the solid contact between the rotor and the bearings. Note that after about three seconds of integration, the rotor at the bottom bearing location actually becomes recentered, having a whirl amplitude of around 0.2 mm peak-to-peak (0.008 in peak-to-peak). This recentering occurs due to the relatively significant direct stiffness coming from the damper seal located at the very bottom of the compressor assembly. The top and middle rotor locations continue to contact the catcher bearing races with a final whirl amplitude of about 0.4 mm peak-to-peak (0.016 in peak-to-peak).

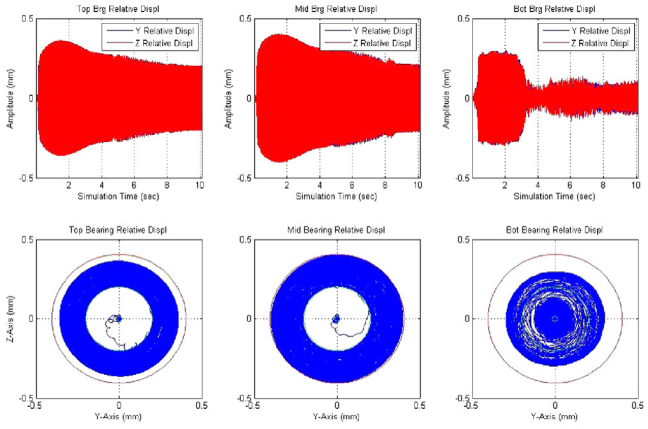

Figure 16. Design Case Predicted Time History.

The waterfall summary in Figure 17 shows this same predicted behavior very clearly. At the beginning of the simulation, the rotor is whirling at a 68 Hz. At about three seconds, the bottom end of the rotor is recentered, no longer whirling at significant amplitude. Also, the rotor whirl frequency is trending down, passing through the third structural mode at 36 Hz and finally ending at 22 Hz forward whirl by the end of the simulation.

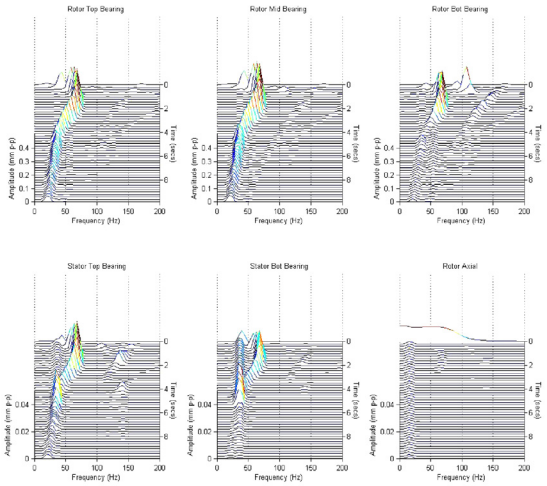

Figure 17. Design Case Predicted Waterfall Summary.

The predicted radial bearing loads for the design case are provided in Figure18. In this plot, the top and middle bearings are shown to experience the highest loads, which occur during the period of whirl at about 68 Hz. As the whirl frequency decays, the loads are reduced exponentially. The bottom bearing loads remain negligible during the entire time, in part due to the relatively strong gas forces present at the damper seal.

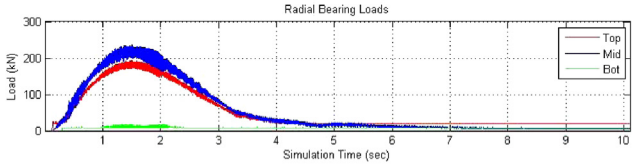

Figure 18. Design Case Predicted Radial Bearing Loads.

Parametric Study Results

A full parametric study is performed to vary the major parameters that might influence the simulation results. These include friction coefficients, catcher bearing preload, unbalance mass, damper ribbon performance, catcher bearing clearance, and applied cross-coupled stiffness (Table 6). For each of these parametric cases, the time history and waterfall plots are found to be very similar. In other words, the system is not largely sensitive to reasonable ranges for any of the tested parameters. However, there is a noticeable difference in each case when viewed from the perspective of peak bearing loads.

Table 6. Full Scale Simulation Parametric Cases.

Case	Description
1	Design Case – All values nominal
2	Reduced friction coefficients
3	Reduced catcher bearing preload
4	Reduced unbalance
5	Reduced damper ribbon performance
6-10	Varying amounts of cross-coupled stiffness
11-12	Reduced catcher bearing clearance

Figure 19 is a plot of calculated peak catcher bearing loads for each of the cases evaluated. The static load rating for the top and middle bearings is 394 kN (88,575 lbf), while for the bottom bearing it is 88 kN (19,783 lbf). These lines are shown in the figure as dashed red and blue lines. The first case (Case 1) is the design case shown above. Cases 2 through 4 are slight variations that result in no noticeable change. Case 5 shows the influence of reduced damper ribbon performance which directly correlates to an increase in bearing load.

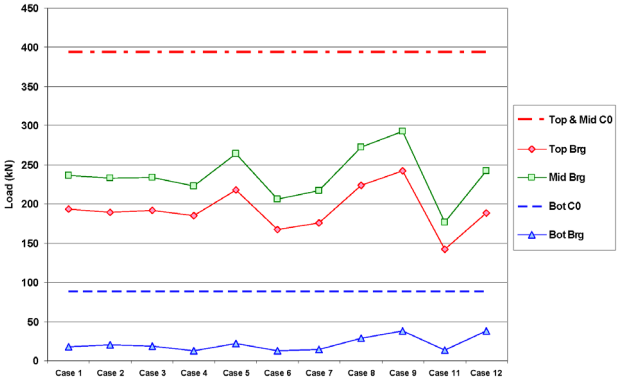

Figure 19. Summary of Predicted Peak Catcher Bearing Loads.

Cases 6 through 10 represent increasing amounts of overall system cross-coupled stiffness. For Case 6, the net cross-coupled stiffness is reduced by 18 MN/m (103 klbf/in) clearly leading to a reduction in peak bearing loads. Table 7 lists the remaining cross-coupled stiffness variations evaluated. As shown by the peak loads, the increasing amounts of cross-coupled stiffness lead to increased bearing loads until finally in Case 10, the system experiences a runaway condition resulting in excessive loads (not plotted). To put this in terms of API stability margin, the additional cross-coupled stiffness required to drive the system unstable is a factor of 2.8 larger than the anticipated impeller cross-coupled stiffness value. This is encouraging, especially for a detailed simulation including all significant rotordynamic components.

Table 7. Impeller Cross-Coupled Stiffness Variations.

Case	ΔKxy (N/μm)	Net Impeller Kxy (N/μm)
Case 1	0	7.89
Case 6	-18	-10.11
Case 7	-9	-1.11
Case 8	+9	16.89
Case 9	+12	19.89
Case 10	+14	21.89
Case 11	0	7.89
Case 12	+14	21.89

Cases 11 and 12 are unique in that the dead-band clearance within the catcher bearing is reduced from 0.200 mm (0.008 in) radial to 0.150 mm (0.006 in). This reduced clearance has the effect of reducing the whirl amplitude just by geometric constraint alone. In addition, since cross-coupled forces are proportional to displacement, the resulting tangential forces are reduced as well. The end result is a noticeable reduction in peak bearing load. Case 11 has the same cross-coupled stiffness as Case 1, but the peak radial load is reduced by about 70 kN (15.7 klbf) for the top and middle bearings. Case 12 has the same cross-coupled stiffness as Case 10, but instead of experiencing runaway amplitudes, the peak bearing loads are limited to about 250 kN (56.2 klbf) at the top bearing location.

SUBSCALE ENDURANCE TESTING

The final portion of the experimental program is an endurance test of the catcher bearing system. The goal of this test series is to identify the number of full speed drops the catcher bearings can withstand prior to failure, and to identify methods that can be used to assess the health of the bearings in the full scale machine. Therefore, for this activity, each of the bearings is instrumented with a microphone, accelerometer, and an embedded resistance temperature detector (RTD) near the catcher bearing outer race. Figure 20 shows the applied instruments installed on a typical catcher bearing cartridge. In addition to these measured parameters, two more criteria are evaluated as well. The first is a bump check that can provide some indication of bearing wear. The second is a coastdown check in which the time to coast freely from 4500 rpm to 4000 rpm is recorded after each full speed drop event.

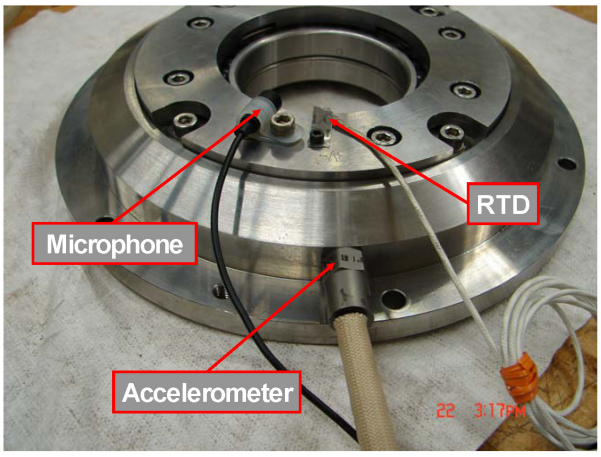

Figure 20. Catcher Bearing Health Monitoring Instruments.

The endurance test program is performed two times, each time with a new set of catcher bearing components (angular contact bearings and damper ribbons). The tests are performed with about 12×API unbalance and are initiated at 30,000 rpm. All axes are delevitated while speed is held constant. Following each full speed landing event (lasting 10 seconds each), a low speed drop is performed to obtain the coastdown test data described above. In addition, a bump check is performed prior to each landing event by statically moving the rotor within the full clearance of the catcher bearings using the AMB. The bump check results for the first test series are provided in Figure 21. There is a significant amount of scatter in the results, so it is careless to make any final conclusions from these data. However, it does appear that there is a trend toward increasing bearing clearance up through Test 7.

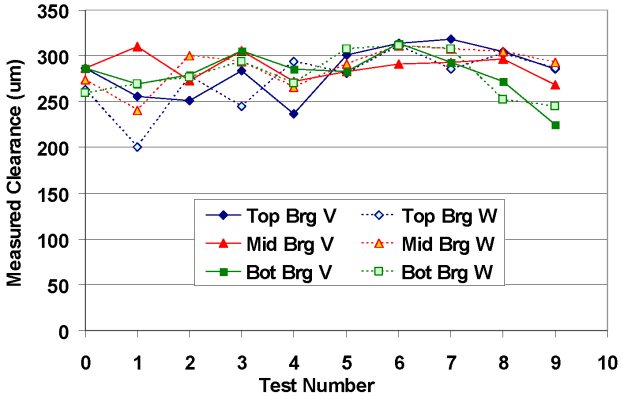

Figure 21. First Series Bump Check Results.

The coastdown results are provided in Figure 22. It is interesting to note that the general trend in the coastdown data is increasing coastdown time. This suggests the resistance to rotation is decreasing, not increasing as anticipated. The authors propose two possible explanations:

- The increase in coastdown time reflects a decrease in angular contact bearing preload. This decrease in preload occurs due to the wearing away of the dry film lubricant that protects the bearings from wear.
- The increase in coastdown time reflects a lapping of the races, which reduces the friction force after each drop.

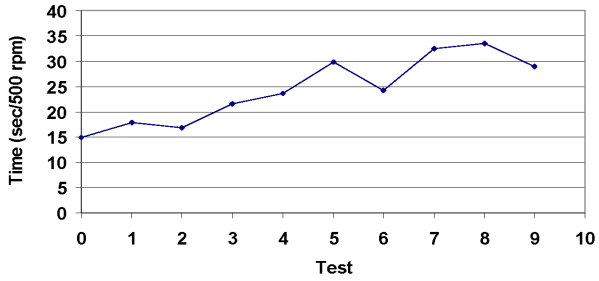

Figure 22. First Series Coastdown Results.

There were a total of 10 full speed drop tests, but due to catastrophic bearing failure during the last full speed drop, there is no coastdown result available for Test 10. Regardless of the mechanism for increasing coastdown time, it is clear that these criteria are difficult to apply on a test-by-test basis. As long as the coastdown time is compared to the original baseline, it may serve as a practical method for anticipating bearing failure.

Data collected from the full speed landings include catcher bearing housing acceleration, catcher bearing outer race temperature, and catcher bearing cavity acoustic emissions. The acoustic emission data are found to be of limited value, and are not presented in this summary. However, the accelerometer and temperature data prove to be practical indicators of impending bearing failure. For the first test series, the accelerometer root mean square (RMS) values are plotted for the duration of each landing test (Figure 23). Each of these tests is initiated at 30,000 rpm and lasts for 10 seconds. For the first eight tests, there is very little acceleration above about 5 g-rms except for the initial response to the drop event. However, during Test 9, there is a striking increase in measured acceleration. This precedes the total bearing failure experience in Test 10, which is noticeable by the excessive accelerations from the very beginning of this last drop. It should be mentioned that since the speed is held constant, the peaks shown in Figure 23 are not resonances but are due to roughness from the damaged areas.

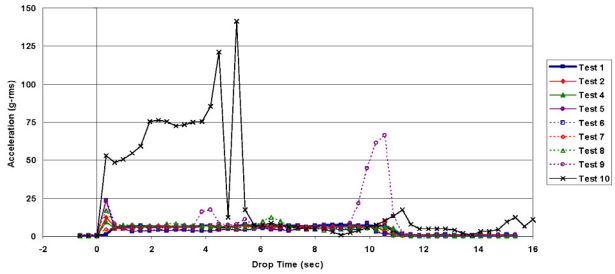

Figure 23. First Series Top Bearing Accelerations.

The RTD data recorded during the full speed drop events is presented in Figure24 for the top bearing. The data are presented as a Delta-T, showing only the change in temperature during the test. Nominally, all bearings started out with a temperature of around 77°F (25°C). The top bearing data are more difficult to view due to the excessive temperatures recorded during the final test, but clearly the first seven tests are tightly grouped, with a maximum temperature

increase of around 68°F (20°C) during the test. The peak also occurs after relevitation, which is likely due to a time delay in the RTD measurement. Tests 8 and 9 demonstrate a gradual increase in outer race temperature, whereas Test 10 shows a maximum temperature increase of almost 320°F (160°C) due to catastrophic damage.

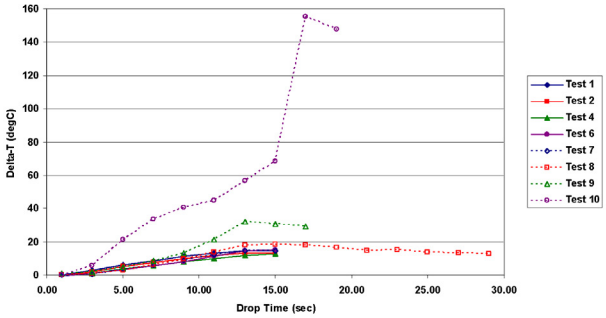

Figure 24. First Series Top Bearing RTD Data.

The second set of full speed drop tests results is found to be very similar to the first series. Figure 25 provides both the endurance Series 1 and 2 results for comparison. Note that the baseline vibration levels are both around 5 g-rms, with the same initial spike up to about 30 g-rms. The first significant increase in top bearing acceleration for the second series occurs during Test 8 and is surprisingly similar to the measured accelerations for Test 9 of the first endurance test series. This perhaps is a strong indication that the top bearing is very close to failure. Based on this result, the second endurance test series is discontinued after Test 8 so as not to repeat the total bearing failure experienced during the first test series.

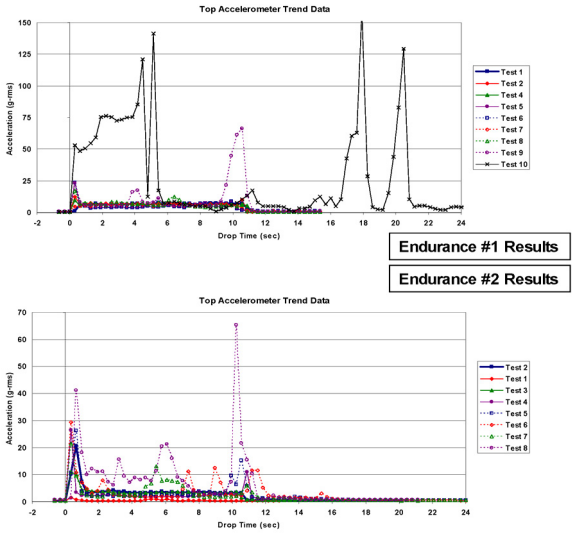

Figure 25. Comparison of First and Second Series.

CONCLUSIONS

This combined experimental/analytical program has provided valuable information that has supported the design of the full scale subsea motor-compressor unit. The test rig designed and built for this program has been successfully used to accomplish the goals set out at the beginning of the project. The first portion of the experimental work is focused on parametric study of the rotordynamic behavior as a function of several variables. Experimental results show that there is very little sensitivity to the magnitude and distribution of the unbalance. In all cases, the whirl is established at about 68 Hz, is in the forward direction (same as direction of spin), and is cylindrical in shape.

Another important result of this work is the overall performance of the catcher bearing system. In all of the parametric studies, the catcher bearings were able to contain the rotor and prevent contact with any of the AMB stator components. This is true even when passing through the rotor bending frequency. In addition, the presence of structural modes within the operating speed range is demonstrated to have no influence on the whirl of the rotor. This is encouraging news as the full-scale machine is anticipated to have structural modes within the operating speed range.

Using the simulation tool that is tuned from the experimental results, the full-scale machine is analyzed for a variety of parametric cases. The simulations predict the machine to be stable for all of these conditions with a margin of more than 2.0. The simulation shows that further improvement in landing dynamic behavior and bearing loads can be found in reducing the total aerodynamic cross-coupled stiffness through the application of anti-swirl devices.

The endurance testing is also completed successfully and demonstrates the capability of the subscale catcher bearings to withstand a minimum of seven full speed landings lasting 10 seconds each. This is encouraging as well, since the full scale machine will decrease from 10,160 rpm down to about 2000 rpm within this same amount of time.

REFERENCES

API Standard 617, 2002, "Axial and Centrifugal Compressors and Expander-Compressors for Petroleum, Chemical and Gas Industry Services," Seventh Edition, American Petroleum Institute, Washington, D.C.

Caprio, M. T., et al., 2004, "Spin Commissioning and Drop Tests of a 130 kW-hr Composite Flywheel," Ninth International Symposium on Magnetic Bearings.

Glasgow, D. A. and Nelson, H. D., 1980, "Stability Analysis of Rotor-Bearings Systems Using Component Mode Synthesis," ASME Journal of Mechanical Design, *102*, (2), pp. 352-359.

Harris, T. A., 1984, *Rolling Bearing Analysis, Second Edition*, John Wiley and Sons, pp. 426-432.

McMullen, et al., 2006, "Flywheel Energy Storage System with AMBs and Hybrid Backup Bearings," Tenth International Symposium on Magnetic Bearings.

Moore, J. J., Ransom, D. L., and Viana, F., 2007, "Rotordynamic Force Prediction of Centrifugal Compressor Impellers Using Computational Fluid Dynamics," ASME Paper No. GT2007-28181.

Ransom, D. L., 2008, "Leveraging the Strengths of Commercial Finite Element Modeling Codes and Custom Engineered Software to Solve Atypical Rotordynamic Problems," ASME TurboExpo.

Ransom, D., Masala, A., Moore, J. J., Vannini, G., and Camatti, M., 2008, "Numerical and Experimental Simulation of a Vertical High Speed Motorcompressor Rotor Drop onto Catcher Bearings," 11th International Symposium on Magnetic Bearings, Nara, Japan, August 26-29.

Schmied, J. and Pradetto, J. C., 1992, "Behavior of a One Ton Rotor Being Dropped into Auxiliary Bearings," Third International Symposium on Magnetic Bearings.

Sun, G., et al., 2004, "Detailed Ball Bearing Model for Magnetic Suspension Auxiliary Service," Journal of Sound and Vibration-269.

Swanson, E. E., Kirk, R. G., and Wang, J., 1995, "AMB Rotor Drop Initial Transient on Ball and Solid Bearings," UVA MAG.

Vance, J. M., 1988, *Rotordynamics of Turbomachinery*, John Wiley & Sons Inc.